SpezialForschungsBereich F 32

Karl–Franzens Universität Graz
Technische Universität Graz
Medizinische Universität Graz

Characterisation of the influence of regularisation methods on the theoretical limits of resolution and contrast to noise ratio for diffusion optical tomography

Manuel Freiberger Robert Merwa

Hermann Scharfetter

SFB-Report No. 2008–012 October 2008

A–8010 GRAZ, HEINRICHSTRASSE 36, AUSTRIA

Supported by the
Austrian Science Fund (FWF)

Der Wissenschaftsfonds.

SFB sponsors:

- **Austrian Science Fund** (FWF)
- **University of Graz**
- **Graz University of Technology**
- **Medical University of Graz**
- **Government of Styria**
- **City of Graz**

Characterisation of the influence of regularisation methods on the theoretical limits of resolution and contrast to noise ratio for diffusion optical tomography

Manuel Freiberger,* Robert Merwa, and Hermann Scharfetter

Graz University of Technology, Institute of Medical Engineering,

Kronesgasse 5, 8010 Graz, Austria

(Dated: September 25, 2008)

Abstract

Diffusion optical tomography is an emerging modality able to provide functional images of physiological processes. In this paper the influence of different regularisation strategies (identity matrix, truncated SVD, neighbouring matrix and variance uniformisation) on quality measures like resolution and contrast to noise ratio is investigated. The estimation of the quality measures is based on Baysian probability theory and simulations carried out with a finite element discretisation of the diffusion equation. The results show that although the neighbouring matrix has a high CNR, its resolution is quite poor. Both truncated SVD and variance uniformisation perform good near the surface but lack resolution in deeper regions. The identity matrix regularisation works also well in deeper regions but has a lower CNR when compared to the other methods.

*Electronic address: manuel.freiberger@TUGraz.at

I. INTRODUCTION

Functional imaging is a rapidly emerging branch in medicine as we strive towards understanding physiological processes in more detail. This has led to developments like photon emission tomography (PET) and functional magnetic resonance imaging (fMRI) but also optical imaging techniques attract interest. The latter ones have the advantage that they do not deal with ionising and thus harmful radiation and that they are not as bulky and expensive as fMRI.

In diffusion optical tomography (DOT) a set of light sources and a set of detectors are placed on the sample. The amount of light travelling from each source to each detector is measured. This can be achieved either by switching the sources sequentially or by modulating them with a distinct set of frequencies and a demodulation at the detector sites. From the attenuation between all source/detector pairs a 3D reconstruction of either the scattering or the absorption coefficient or some other derived parameter inside the sample can be calculated.

In order to compare different imaging techniques, devices and setups, some characteristic quantities like resolution, contrast to noise ratio and minimum detectable object size come in handy. The aim of the current paper is to investigate how much different regularisation methods for DOT single-step reconstruction influence these quantities.

II. METHODS

A. Forward and inverse problem

To describe the propagation of light in tissue, Boltzmann's transport equation can be used. However, often it is not feasible to deal with this equation directly as this would require a lot of computing effort.

For materials which are much more scattering than absorbing, as it is the case for many biological tissues, the diffusion model is a good approximation. This model is given by the partial differential equation (PDE)

$$-\nabla \cdot (\kappa \nabla \phi) + \left(\mu_a + \frac{i\omega}{c} \right) \phi = s, \tag{1}$$

together with the Robin-type boundary condition

$$\phi + 2R\kappa\frac{\partial\phi}{\partial n} = 0 \tag{2}$$

where ϕ is the photon density, $\kappa = (3(\mu_a + \mu_s'))^{-1}$ the diffusion coefficient, μ_a the absorption coefficient, μ_s' the reduced scattering coefficient, ω the modulation frequency of the light, c the speed of light in the medium, s the source term, and R a factor incorporating the reflection at the boundary. A derivation of this equation from the transport equation can be found in [1]. The variational formulation of the problem above can be solved efficiently using a finite element method.

Within this paper the focus is on the reconstruction of the absorbtion parameter, which shall be constant within a finite element. The vector of all absorption coefficients is written as m. Further, the scattering parameter is assumed to be known and constant. The Jacobian or sensitivity matrix S is calculated with an adjoint approach [1]. Let ψ be the solution to the adjoint problem of the PDE above. V_k denotes a basis system matrix for the absorbtion coefficient in the k-th element. Then the sensitivity of the j-th source/detector pair in the k-th element can be written as

$$S_{jk} = -\langle \psi_{d(j)}, V_k\, \phi_{s(j)} \rangle, \tag{3}$$

whereby $d(j)$ and $s(j)$ are the indices of the detector and source of the j-th measurement and $\langle\cdot\rangle$ is the inner product.

Throughout this paper only difference measurements will be used. That means a reference measurement d_0 is made on an object with given background parameters m_0 and a second measurement $d = d_0 + \Delta d$ on the same object but with perturbed absorption parameters $m = m_0 + \Delta m$ is performed. If the change in the absorption parameters is small, the change in the measurement can be approximated by a first-order Taylor series expansion with the sensitivity matrix:

$$\Delta d = S\Delta m \tag{4}$$

For some reconstruction methods, a singular value decomposition (SVD) of the sensitivity matrix is required. At this point the SVD is defined to be $S = U\Sigma V^t$, where the matrix U contains the basis vector of the data space, V contains the basis for the model space and Σ is a diagonal matrix containing the singular values.

B. Reconstruction methods

The inverse problem of (4) is to reconstruct a vector of parameters $\Delta\widetilde{m}$ from a vector of measurements Δd. This is a highly underdetermined problem as often around 10^5 voxels have to be reconstructed from only some 100 measurements. The reconstructed parameters are given by the equation

$$\Delta\widetilde{m} = S^t(SS^t)^{-1}\Delta d \tag{5}$$

which is called the minimum-length solution, *i.e.* it gives the one parameter vector which satisfies $S\Delta\widetilde{m} = \Delta d$ exactly and at the same time has the smallest norm. Unfortunately, this solution is not stable due to the ill-posedness of the problem, which leads to a poor conditioning of $(SS^t)^{-1}$ and an unstable inversion, thus.

A stable solution can obtained through minimising the weighted least-squares functional

$$\Psi(\Delta m) = (S\Delta m - \Delta d)^t C_D^{-1}(S\Delta m - \Delta d) + \Delta m^t M^t M \Delta m \tag{6}$$

whereby C_D is the covariance matrix of the data and $m^t M^t M m$ is a Tikhonov regularisation term. The last term enters *a-priori* information on the behaviour of the parameters to improve the conditioning.

The same result can be obtained using a Bayesian approach for inversion. It has the additional advantage that a clear physical interpretation of the regularisation term can be given. In this paper, the *a-priori* model parameters Δm shall have a Gaussian distribution centered at Δm_0 with a covariance matrix C_M. Also, the distribution of measurements shall be Gaussian with a center at Δd (*i.e.* at the actual value recorded) and a covariance matrix C_D. It can be shown [2] that the best estimate in the least-squares sense for the reconstructed model parameters is given by

$$\Delta\widetilde{m} = \Delta m_0 + C_M S^t \left(SC_M S^t + C_D\right)^{-1} (\Delta d - S\Delta m_0) \tag{7}$$

together with the *a-posteriori* covariance matrix

$$\widetilde{C}_M = C_M - C_M S^t \left(SC_M S^t + C_D\right)^{-1} SC_M. \tag{8}$$

As the focus lies on the reconstruction of the perturbation, Δm_0 is set to 0 from now on. A further abbreviation is to introduce the pseudo-inverse as $S^\dagger := C_M S^t \left(SC_M S^t + C_D\right)^{-1}$. Also, we want to stress that essentially the same result would have been obtained by choosing

the matrix M in the Tikhonov regularisation term to be $M^tM = C_M^{-1}$ but Bayesian theory offers a better physical interpretation.

C_D is fixed as it is determined by the noise of the detector system. The detector noise shall be uncorrelated so that one can write $C_D = \sigma_D^2 I$. The only quantity not yet fixed is the *a-priori* covariance matrix C_M. Several regularisation schemes are common which lead to different choices of the covariance matrix. The following were investigated:

- Identity matrix ($C_M = \lambda I$): The covariance is simply chosen as a scaled identity matrix which means that *a-priori* all the parameters have the same distribution and are independent of each other. High values of the reconstructed parameters are penalised.

- Neighbouring matrix ($C_M^{-1} = \lambda N_M$): The identity matrix has the drawback that relatively high parameters are penalised although in reality high differences of parameters in different compartments (*e.g.* absorption in different organs) may be sensible and are expected. Often a more realistic choice is to demand that a parameter does not differ very much between adjacent voxels. This behaviour can be achieved with a spatial filter like the neighbouring matrix:

$$(N_M)_{ij} = \begin{cases} n_i + \varepsilon & \text{if } i = j \\ -1 & \text{if elements } i \text{ and } j \\ & \text{share a facet} \\ 0 & \text{else} \end{cases} \tag{9}$$

  where n_i denotes the number of neighbours of the i-th element and ε is a small positive constant which is necessary as the matrix would be singular otherwise.

- Truncated SVD ($C_M = V\lambda I_T V^t$, $\lambda \to \infty$): The problem when inverting $(SS^t)^{-1}$ is the poor condition number of S. A truncated SVD skips all singular values that are below a threshold ε or equivalently skips all singular values above an appropriately chosen index T. This behaviour can be achieved by setting $C_M = V\lambda I_T V^t$, where $\lambda \to \infty$ and I_T is a truncated identity matrix, *i.e.* $(I_T)_{ij} = 1$ for $i = j \wedge i <= T$ and 0 else. A derivation can be found in the appendix A.

- Variance uniformisation ($C_M^{-1} = VDV^t$): Cohen-Bacrie *et al* proposed to choose the *a-priori* covariance matrix so that the *a-posteriori* covariance is uniform in the whole

region [3]. This is possible, if the matrix D is set to

$$D = (\lambda\Sigma - \Sigma^2)I_T, \tag{10}$$

where λ is a regularisation parameter and I_T is again a truncated identity matrix which is included for stability reasons only.

C. Optimisation of regularisation parameters

All regularisation methods introduced above require the tuning of one or more parameters. IM and NM depend on the parameter λ, tSVD depends on the choice of the truncation level T and VU is dependent on both. Choosing small values for λ or high values for T results in almost no regularisation, while the choice of big values for λ and small values for T causes the reconstructed image to be very smooth.

In literature several methods are well established in order to optimise the regularisation parameter, amongst them the L-curve criterion, the gerneralised cross-validation, and Morozov's discrepancy principle. L-curves often have the problem that they do not show a proper L-shape with a distinct corner but are quite smooth instead which makes it hard to choose the correct parameter. This makes the latter two methods a better choice.

Morozov's discrepancy principle states that the error due to the regularisation should be in the order of the error due to measurement noise [4]. The regularisation error can be calculated by making a forward simulation with the parameters obtained from the reconstruction:

$$\|S\widetilde{m} - d^{\delta}\| = \sigma_D, \tag{11}$$

with d^{δ} being the noisy measurement data. Due to its clear physical interpretation it was the preferred method in the work done by Scharfetter *et al* [5] and is also used in here.

D. Simulation model

All FE simulations were performed on a cylinder with a diameter of 30 mm and a height of 90 mm (see figure 1). The mesh was built up of approximately 292,000 tetrahedrons. Around the cylinder 16 point sources and 16 point detectors were placed in a zig-zag arrangement on two rings separated by 25 mm. This configuration was chosen in order to avoid a symmetry

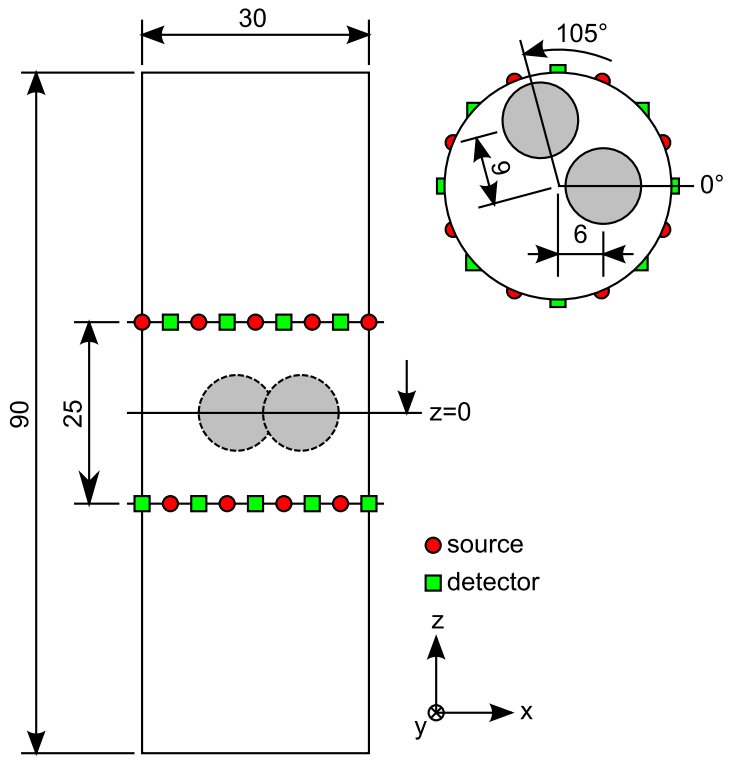

FIG. 1: Simulation model with frontal view (left) and transversal cross-section through the middle of the cylinder. All measurements in mm. See the text for details.

plane at $z = 0\,\text{mm}$ which could lead to an ambiguity of the perturbation's location in the reconstruction. The background scattering and absorption were set to $\mu_s' = 0.5\,\text{mm}^{-1}$ and $\mu_a = 0.1\,\text{mm}^{-1}$. These values were taken from [6] and approximate lumped tissue. The index of refraction was set to $n = 1.36$, which is an average value for most tissue types. The refraction factor R was calculated using the equation derived by Keijzer *et al* [7].

Inside the cylinder two sphere-shaped perturbations with a radius of 5 mm were placed at locations (r=6 mm, φ=0°, z=0 mm) and (r=9 mm, φ=105°, z=0 mm). The absorption coefficient was increased by 10 % inside them.

The light source used in the simulation was a point source with a wavelength of 630 nm and an output power of 2 mW. Also, the detectors were modelled to be point detectors. Further, it was assumed that all detectors exhibited uncorrelated Gaussian noise with zero mean. Its standard deviation was set to -130 dBW, -135 dBW and -140 dBW, which is achievable with high-quality avalanche photodiode modules.

All reconstructions were performed on another mesh with the same outer dimensions but only 103,000 tetrahedral elements.

E. Resolution

Resolution is an important quality criterion for imaging techniques as it is a measure for the amount of objects resolvable per length. It is closely related to the point-spread function (PSF), which is the reconstruction of a theroretically point-shaped perturbation.

To characterise the resolution of the system, a full-width half-maximum (FWHM) criterion is used. Thus, two point-shaped perturbations can be separated if the maximum of their PSF are separated by the 50 %-width of their PSF. In contrast to other common medical imaging modalities like CT or MR, the resolution of DOT is not spatially invariant which is also true for other diffusion-dominated methods like electrical impedance tomography or magnetic induction tomography. It depends on the sample geometry, the source/detector configuration, and the location of the perturbation. Accordingly it is necessary to evaluate the resolution in every point and to create a resolution map.

Another problem is that resolution in DOT is not isotropic as the 50 %-boundary of a PSF is not necessarily a sphere. Therefore, an ellipsoid is fitted to the 50 %-boundary PSF and the largest diameter is taken as the PSF's FWHM which corresponds to the worst case resolution.

F. Contrast to noise ratio

Another quality measure for imaging methods is the constrast-to-noise ratio (CNR), which relates the value of the reconstructed parameter to the uncertainty in the reconstruction. It is a measure for the ability to discriminate one object from its background.

Actually, we would like to use a Weber contrast $C = (\Delta\widetilde{m}_{pert} - \Delta\widetilde{m}_0)/\Delta\widetilde{m}_0$, whereby $\Delta\widetilde{m}_{pert}$ and $\Delta\widetilde{m}_0$ are the reconstructed parameters in the perturbation and the background, respectively. This definition is, however, not feasibly as $\Delta\widetilde{m}_0 = 0$ due to the difference measurements. So the contrast used in this paper is simply the difference $C := \Delta\widetilde{m}_{pert} - \Delta\widetilde{m}_0 = \Delta\widetilde{m}_{pert}$.

In the simulations the contrast was calculated by averaging the value of the reconstructed parameter inside the perturbation. Let the mask vector h be defined as

$$h_i = \begin{cases} 1 & \text{if the } i\text{-th element is inside the perturbation} \\ 0 & \text{else} \end{cases} \tag{12}$$

in order to specify the location, shape and size of the perturbation. Δm_{pert} shall be the true value of the parameter inside the perturbation. After a reconstruction the perturbation will likely be shifted and distorted which is why we also define an *a-posteriori* mask vector $\tilde{h}$. Analogous to equation (12), $\tilde{h}$ is one for all voxels which satisfy the FWHM criterion presented in the previous section and is zero elsewhere. The contrast is then

$$C = \frac{\tilde{h}^t}{\|\tilde{h}\|_1} S^\dagger S\, h \Delta m_{pert}. \tag{13}$$

The noise n in the reconstruction can be calculated by taking the square root of the sum of the variances and covariances of the voxels inside the reconstructed perturbation:

$$n = \frac{1}{\|\tilde{h}\|_1} \sqrt{\tilde{h}^t \widetilde{C}_M \tilde{h}}\ . \tag{14}$$

As the covariance matrix grows rapidly with increasing post-mask size, the Cauchy-Schwarz inequality comes in handy as it needs the diagonal elements only:

$$n \leq \frac{1}{\|\tilde{h}\|_1} \left(\sum_{i \in \tilde{h}} \sum_{j \in \tilde{h}} \sqrt{(\widetilde{C}_M)_{ii} (\widetilde{C}_M)_{jj}} \right)^{1/2}, \tag{15}$$

where the sums are ment to be over those voxels which belong to the reconstructed perturbation.

Putting equations (13) and (14) together, one obtains finally an expression for the contrast to noise ratio:

$$\mathrm{CNR} = \frac{\tilde{h}^t S^\dagger S\, h \Delta m_{pert}}{\sqrt{\tilde{h}^t \widetilde{C}_M \tilde{h}}} \tag{16}$$

G. Detectability radius

The detectability radius describes how large an object with a given parameter has to be so that the system can still detect it. This quantity is closely linked to the CNR as the detection limit is reached when the contrast to noise ratio is one, *i.e.* when the reconstructed value of the perturbation vanishes in the parameter noise.

In this section a homogeneous FE discretisation is assumed such that all the voxels have approximately the same volume. One can then infer that the volume of the perturbation scales linearly with the amount of voxels inside the perturbation.

Suppose one has a small point-shaped perturbation. In a neighbourhood of this perturbation the sensitivity will be almost constant. This means that the size of the reconstructed perturbation will scale linearly with the size of the true perturbation. Further, one can see from (13) that the contrast will be constant and independent of the volume, too.

Now take a closer look at (14). If all the voxels would be independent, the covariance matrix would be diagonal and the noise would scale inversely with the square root of the number of voxels and with the perturbation's volume, thus. The other extreme is a full covariance matrix with the same correlation for all voxels. In this case the noise would be constant with respect to the volume.

Taking those two considerations together one finds that the CNR is proportional to the volume of the true perturbation taken to some exponent, *i.e.* $\mathrm{CNR} \sim V^{\alpha}$, with an exponential factor $0 \leq \alpha \leq 1/2$.

Now, let V_i denote the volume of a perturbed voxel and CNR_i the resultant contrast to noise ratio. The radius of a sphere whose volume corresponds to a CNR = 1, *i.e.* the detection limit, is given by

$$r_{\mathrm{lim},i} = \left(\frac{3}{4\pi} \frac{V_i}{\mathrm{CNR}_i^{1/\alpha}} \right)^{1/3} \tag{17}$$

and it is called the detectability radius.

III. RESULTS

In table I the regularisation parameters are listed, which were used in order to reconstruct the absorption coefficient.

Figure 2 shows the reconstruction of the two spherical perturbations for a noise level of -130 dBW. The transversal cross-section is through $z = 0$ mm, which is the middle of the cylinder. In order to visualise both perturbations simultaneously, the axial section was angled as is sketched in the left-most cross-section.

A comparison of the reconstruction for the various noise levels used, can be found in figure 3.

Figure 4 depicts the resolution using the tSVD regularisation for different noise levels. As resolution is a spatially variant measure, it was evaluated at 30 equidistant points along the cylinder radius at the height of the upper ring of optodes ($z = 12.5$ mm). To compen-

TABLE I: Regularisation parameters used for the reconstruction with respect to the measurement noise level

	IM[a]	NM[a]	tSVD[b]	VU[c]
-120 dBW			44	
-130 dBW	5.6E-5	2.9E-6	98	96, 5.6E-4
-135 dBW	6.6E-5	7.1E-5	151	153, 4.2E-4
-140 dBW	6.3E-5	1.3E-5	157	157, 4.7E-3
Noise free	n.a.	n.a.	256	n.a.

[a]Parameter λ
[b]Truncation level T
[c]Truncation level T, parameter λ

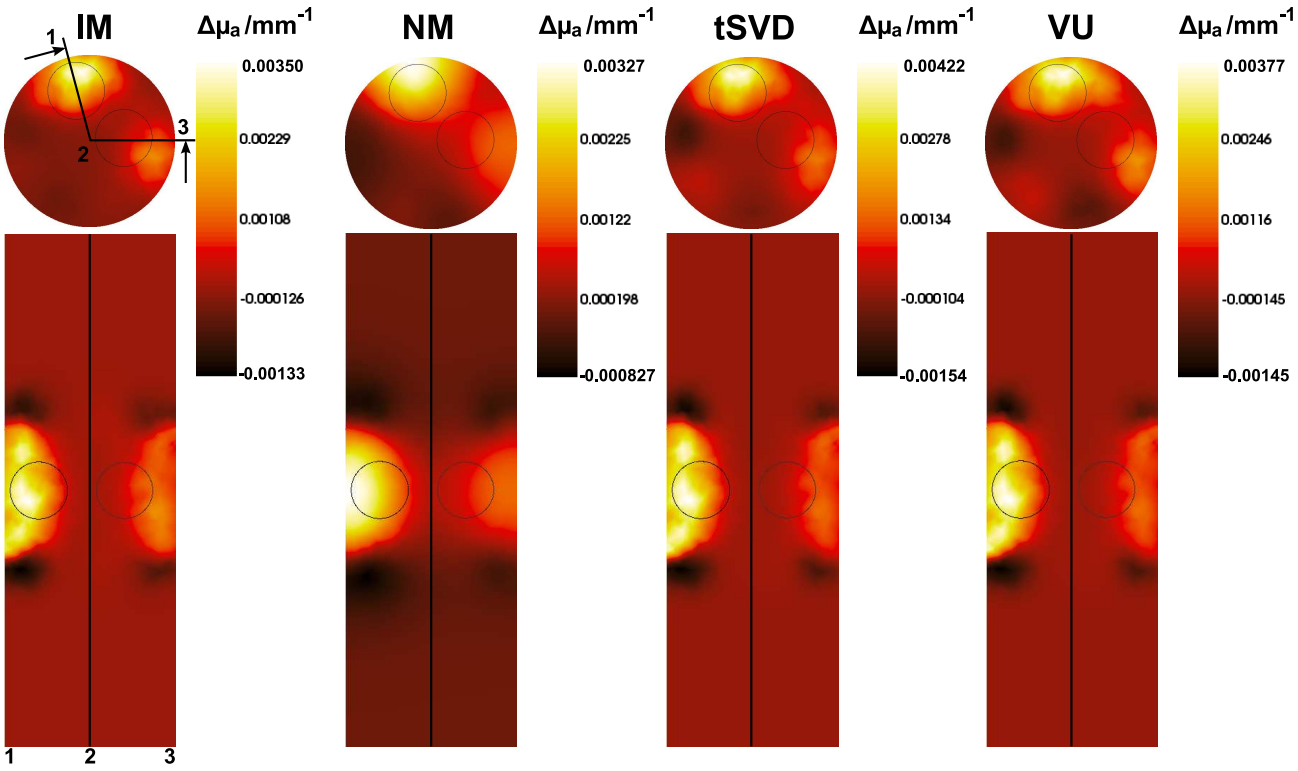

FIG. 2: Reconstruction of two spherical perturbations with 10 % increase in absorption and a noise level of -130 dbW using different regularisation matrices. The axial section was angled (see transversial cross-section in the left-most cylinder) in order to visualise both perturbation simultaneously. The true location of the perturbations is sketched with circles.

sate errors due to the FE discretisation it was further averaged over 64 radii with equal angular spacing . The limit resolution for noise-free data was calculated with the tSVD method without truncating singular values, which means that all data available was used for reconstruction. This is not applicable for the other reconstruction methods as the Morozov criterion cannot be used to determine the optimal regularisation parameter without measurement noise.

Instead of plotting the inverse of the FWHM of the PSF (*i.e.* resolvable points per length), it was chosen to normalise this quantity by the cylinder diameter. Thus, what is plotted in the diagram is actually the amount of points that are resolveable per unit diameter.

The obtainable resolution for a noise level of -130 dBW and its dependence on the regularisation method is shown in figure 5. In some cases pronounced side lobes appeared in the reconstruction which also fulfilled the FWHM criterion. As this caused an artificial reduction in resolution due to the seemingly larger extent of the PSF, the following strategy was used to circumvent this problem: For the calculation of the size of the PSF only voxels in a small region around the PSF's maximum were considered first. When this region was increased also the size of the PSF increased until the region covered that part of the main lobe which fulfilled the FWHM criterion. A further increase of the region led to a constant PSF size until it reached a FWHM conforming side lobe which was followed by a sudden increase of the PSF's extent. To compute the resolution the size of the PSF in the plateau phase was taken.

The contrast to noise ratio was evaluated for a spherical perturbation with a radius of 5 mm and an absorption coefficient of $\Delta\mu_a = 0.01\,\mathrm{mm}^{-1}$, which are exactly the characteristics of the perturbations used already before. This sphere was placed at 30 equally spaced points along the radius at $z = 12.5$ mm and averaged over 64 radii again.

In order to compute the detectability limit, the exponential scaling factor in equation (17) had to be estimated first. A parameter fitting on some simulations showed that α was in the range 0.38–0.45 using IM or NM as regularisation methods. However, when the regularisation was switched to tSVD or VU the CNR scaled only with $\alpha \approx 0.03$. Therefore, it was decided to calculate the detectability radius only for IM and NM with $\alpha = 0.35$. The result can be found in figure 7.

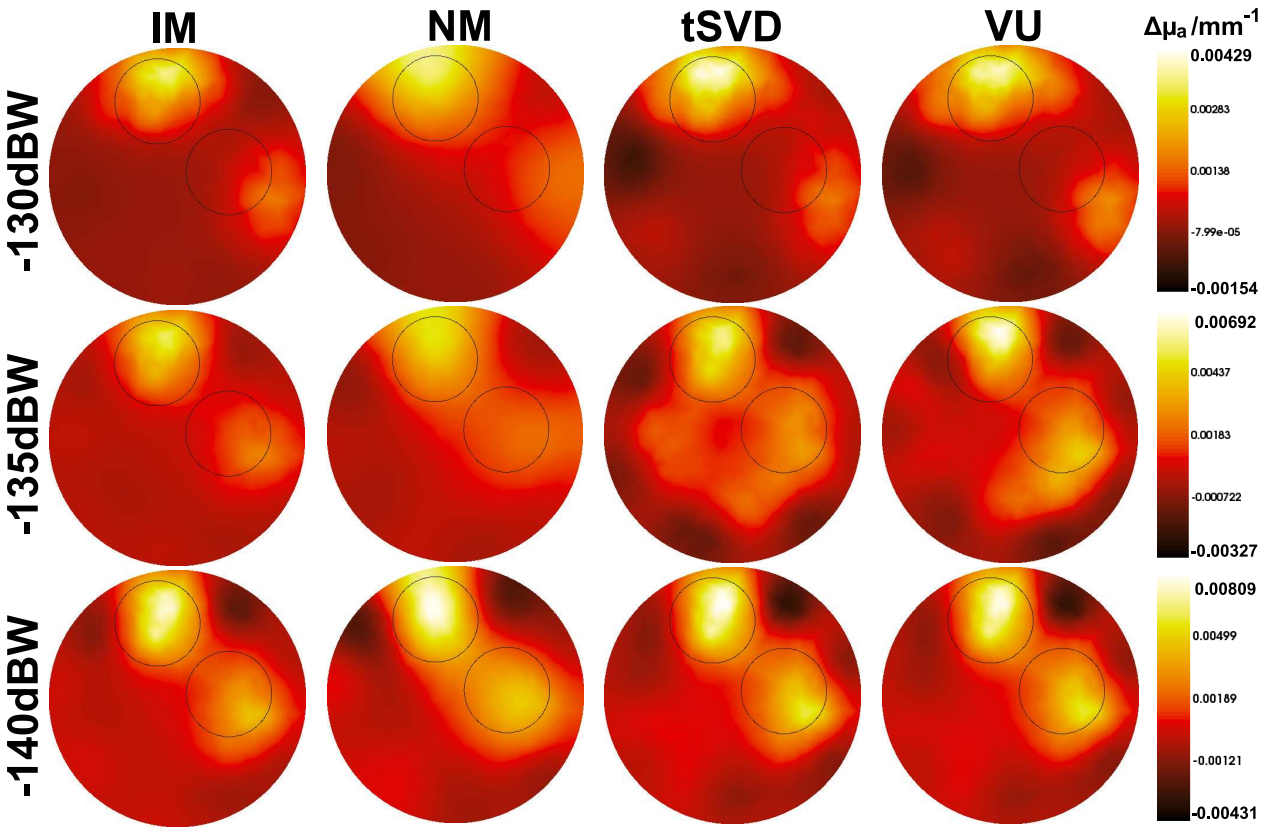

FIG. 3: Transversal reconstructions at $z = 0$ for different noise levels and different regularisation methods.

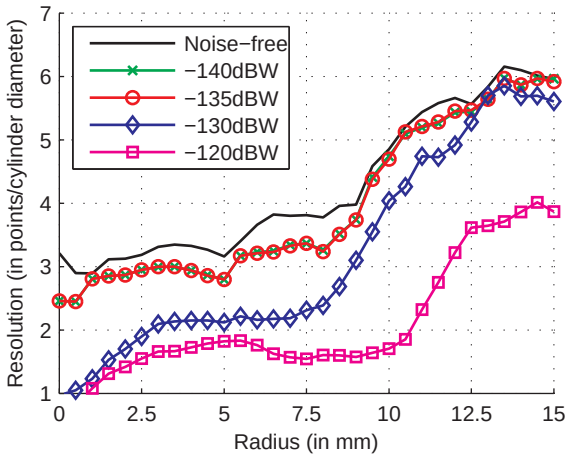

FIG. 4: Resolution along the cylinder radius for different noise-levels using tSVD. The black line without markers shows the resolution for noise-free data obtained without truncating singular values.

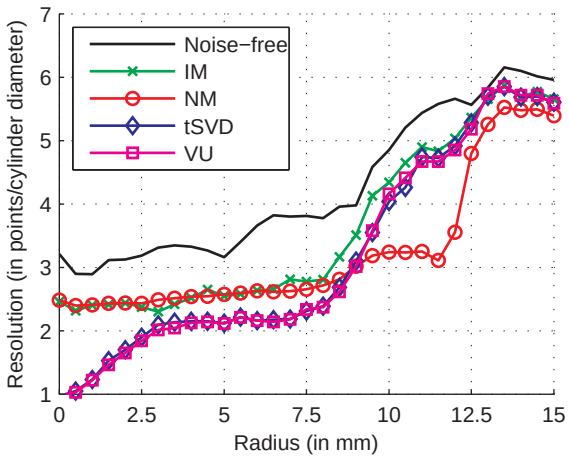

FIG. 5: Resolution for different reconstruction methods. The line without markers shows the maximum theoretical resolution. The noise level for all other graphs was set to -130 dBW.

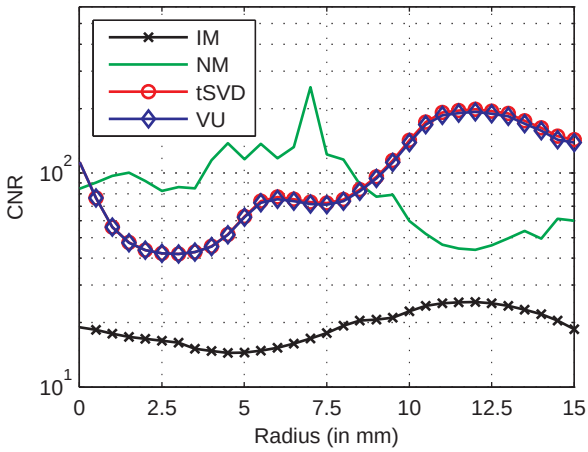

FIG. 6: Contrast to noise ratio for a spherical perturbation with a radius of 5 mm and an absorption difference $\Delta\mu_a = 0.01\,\mathrm{mm}^{-1}$ placed equally spaced along the cylinder radius at $z = 12.5$ mm. The measurement noise level was set to -135 dBW.

IV. DISCUSSION

It can be seen in figure 2 that IM, VU and tSVD produce nearly identical images except the fact that the maximum value of the reconstructed absorption is slightly different and IM tends to separate the perturbations a bit more clearly. They have in common, that the perturbation near to the surface is reconstructed better than the deeper one. Also, it can be noticed that the perturbations are shifted towards the cylinder boundary.

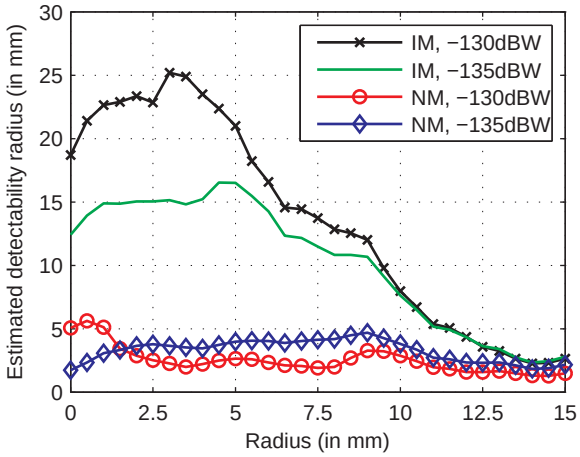

FIG. 7: Estimated detectability radius along the cylinder radius for a perturbation with a difference in absorption coefficient of $\Delta\mu_a = 0.01\,\mathrm{mm}^{-1}$ using identity and neighbouring matrix regularisation at different noise levels.

Using NM as regularisation, the image gets much smoother and the boundaries of the perturbations are in some sense more regular. Mathematically this behaviour can be explained by the fact that the neighbouring matrix is a regularisation matrix from the Sobolev space H^1, which means that an additional smoothness constrained is applied on the parameter's gradient. Further it can be seen in the transversal cross-sections that this method shifts the perturbation even more to the boundary.

At a noise level of -135 dBW using tSVD strong ringing artifacts can be seen in the image (figure 3). Although they are also present in the VU image, they are not as pronounced there. In such a case, the smoothing of IM or NM is certainly advantageous.

Comparing the transversal cross-sections for different noise levels (first to third row in figure 3), it can be concluded that the size and location of the perturbations get more accurate for lower noise levels. This is common for all regularisation methods.

The graphs in figure 4 show that the resolution obtained with tSVD is at best 6 points/diameter near the boundary and only half of it in the middle of the cylinder. As long as the noise level does not exceed -135 dBW this characteristic is preserved. For higher noise the resolution starts to decrease in the deeper regions first. At the surface it stays more or less constant and only decreases at quite high noise levels (see curve for -120 dBW noise).

Comparing the resolution using different regularisation methods one can notice that near

the boundary all methods have more or less the same performance and can resolve around 5.3–6 objects/diameter (figure 5).

The tSVD and VU methods lose resolution near the cylinder's axis. This happens because mainly singular vectors with low singular values are present there and they will be truncated during reconstruction. This is not true for the IM or NM regularisations which show a stable resolution even in deeper regions.

The enforced continuity of the gradient when using the NM method is the reason why the resolution of this regularisation matrix is so poor. It hardly exceeds 2.5 points per unit diameter and cannot resovle objects in depths of 10–12 mm at all.

The fact that the graphs are not very smooth, which can be noticed especially in the noise-free case, is most likely due to the FE discretisation. Thus, better results could be obtained if the geometry was divided into smaller voxels resulting in an increased computational effort.

All graphs also show a decrease in resolution near the cylinder's boundary. This behaviour can be explained by the well-known 'banana-shaped' sensitivity profile of two optodes (see *e.g.* [8]): The sensitivity is highest along a sickle-shaped curve connecting the source and detector optodes. It is not only smaller deeper inside the tissue but also near the surface between the optodes. A loss in sensitivity goes along with a broadening of the reconstructed perturbation and a loss in resolution, thus.

The resolution was also analysed at the median transversal plane of the cylinder where it is quite low. In the noise-free case only around 2–2.5 objects can be resolved while for a noise-level of only -140 dBW it decreases down to approximately 1.3 objects/diameter already. For higher noise, the resolution is below unity, meaning that it is not possible to separate distinct objects any longer.

An interesting result in this study is the contrast to noise ratio of the reconstructed absorption coefficent which is shown in figure 6. As can be seen, tSVD and VU delivered nearly identical results and roughly the same performance as the regularisation using NM with values in the range of 40–195. Those three methods outperform IM by a factor of 2–10 depending on the depth of the perturbation.

Regarding NM the large spread of the reconstructed perturbation is certainly advantageous in this case because the averaging over many voxels reduces the reconstruction noise. In other words, there is a trade-off between a high contrast to noise ratio and a low resolution for this method.

It is also interesting to note that the CNR curve using NM is not as smooth as the curves for the other four regularisation methods. Also it shows a somewhat inverted characteristic and tends to decrease in a depth of 10–12.5 mm where all other methods show an increase in CNR. This behaviour is not yet understood and needs more investigation.

The reason for the good performance of the tSVD and VU methods is that they set the variance of the parameter vector's projection onto the singular vectors with an index smaller than the truncation level to infinity and the rest to zero. In other words, it is assumed that the projections of the *a-priori* model parameters on those singular vectors which correspond to small singular values are already exact. These singular vectors are present mainly deeper inside the cylinder near the axis. As the *a-posteriori* covariance has to be smaller or at least equal to the *a-priori* one, tSVD and VU have inherently a small noise level and a larger CNR, thus.

The steep increase of the CNR curves for tSVD and VU near the cylinder's axis is due to the poor resolution of these regularisation strategies and large extent of the PSF, thus.

The minimum radius such that a spherical perturbation can still be detected gives reasonable results when the identity matrix is used as regularisation strategy (see figure 7). With increasing depth it is more difficult to detect an object and the radius increases, thus. Also, the radius will increase with increasing data noise as it is necessary to average more voxels in order to get a reasonable CNR.

However, this characteristic is not visible when the neighbouring matrix is used instead. The detectability radius is almost constant with respect to depth and noise level. The reason for this is most likely the large spread of the reconstructed perturbation. As it tends to fill most of the cylinder's cross-section the noise decreases due to averaging a large volume. This again leads to a large CNR and the detectability radius when computed using equation (17) will be underestimated.

In all four cases it can be noticed that the detectability radius is lowest some millimetres inside the cylinder. This is again due to the banana-shaped sensitivity distribution of the photons which was already discussed before.

V. CONCLUSION

We have shown the influence of different regularisation strategies for diffusion optical tomography on resolution, CNR and the detectability radius at various noise levels. NM shows a trade-off between resolution and CNR. tSVD and VU both lack resolution in deeper regions. IM tends to be an all-round method working also in deeper regions with a still acceptable CNR.

Acknowledgments

The authors would like to thank Dr. Herbert Egger for the enlightening discussions on this topic.

This work was supported by the SFB F32-N18 granted by the Austrian Science Fund.

APPENDIX A: COVARIANCE MATRIX FOR TSVD

We start with the pseudo-inverse $S^\dagger = C_M S^t \left(S C_M S^t + C_D\right)^{-1}$ and a singular value decomposition of the sensitivity $S = U\Sigma V^t$. V contains the basis vectors of the model space which is why we choose the *a-priori* covariance matrix to be $C_M = VDV^t$ with a diagonal matrix D which is still to be determined. The known data covariance C_D is expressed in terms of U as $C_D = UNU^t$ with a matrix N. We focus on diagonal matrices C_D only, which also renders the matrix N diagonal.

Inserting this into the pseudo-inverse and using the orthonormality relations for U and V as well as the symmetry of Σ, one obtains $S^\dagger = VD\Sigma(\Sigma D\Sigma + N)^{-1}U^t$. As all the matrices in the parantheses are diagonal, we rewrite this as $\mathrm{diag}(\sigma_i^2 d_i + n_i)^{-1}$, whereby σ_i, d_i and n_i denote the diagonal entries of Σ, D and N, respectively. This leads directly to

$$S^\dagger = V\,\mathrm{diag}\left(\frac{\sigma_i d_i}{\sigma_i^2 d_i + n_i}\right) U^t. \tag{A1}$$

No constraint is imposed during reconstruction on the projection of the parameter onto the i-th singular vector, if the *a-priori* variance is chosen to be $d_i \to \infty$. The other extreme is to clamp the reconstruction to the *a-priori* value by choosing the variance to be $d_i = 0$.

A truncated singular value decomposition regularises by setting singular values above a threshold T to zero. This is equivalent to clamping the projection of the parameters onto

the corresponding singular vectors to their initial values during reconstruction. Thus, the *a-priori* covariance matrix is $C_M = V\lambda I_T V^t$ with $\lambda \to \infty$ and a truncated identity matrix I_T.

As one can easily proof, the *a-posteriori* covariance matrix is then given by

$$\widetilde{C}_M = V \,\mathrm{diag}\left(\frac{n_i d_i}{\sigma_i^2 d_i + n_i}\right) V^t. \tag{A2}$$

This means that after reconstruction the error is zero along the singular vectors which were neglected and is limited to n_i/σ_i^2 along those which were not constrained.

---

[1] S. R. Arridge, Inverse Problems **15**, R41 (1999).

[2] A. Tarantola, *Inverse Problem Theory and Methods for Model Parameter Estimation* (SIAM, 2005).

[3] C. Cohen-Bacrie, Y. Goussard, and R. Guardo, IEEE Transactions on Medical Imaging **16**, 562 (1997).

[4] K. Kunisch and J. Zou, Inverse Problems **14**, 1247 (1998).

[5] H. Scharfetter, K. Hollaus, J. Rosell-Ferrer, and R. Merwa, Annals of Biomedical Engineering **34**, 1786 (2006).

[6] J. Mobley and T. Vo-Dinh, in *Biomedical Photonics Handbook*, edited by T. Vo-Dinh (CRC Press LLC, Boca Raton, USA, 2003), pp. 2/1–2/75.

[7] M. Keijzer, W. M. Star, and P. R. M. Storchi, Applied Optics **27**, 1820 (1988).

[8] E. Okada, M. Firbank, M. Schweiger, S. R. Arridge, M. Cope, and D. T. Delpy, Applied Optics **36**, 21 (1997).